Rock and Soil Mechanics

Volume 42 | Issue 6 Article 9

10-22-2021

Fracturing mechanism of rock-like specimens with different joint densities based on DIC technology

Fei-fei QI
Faculty of Civil and Architectural Engineering, Kunming University of Science and Technology, Kunming, Yunnan 650500, China

Ke ZHANG
Faculty of Civil and Architectural Engineering, Kunming University of Science and Technology, Kunming, Yunnan 650500, China, zhangke_csu@163.com

Jian-bin XIE
Department of Civil Engineering, Yunnan University, Kunming, Yunnan 650500, China

Rock and Soil Mechanics 2021 42(6): 1669−1680 ISSN 1000−7598
https: //doi.org/10.16285/j.rsm.2020.6710 rocksoilmech.researchcommons.org/journal

Fracturing mechanism of rock-like specimens with different joint densities based on DIC technology

QI Fei-fei[1, 2], ZHANG Ke[1, 2], XIE Jian-bin[2, 3]

1. Faculty of Electric Power Engineering, Kunming University of Science and Technology, Kunming, Yunnan 650500, China
2. Faculty of Civil and Architectural Engineering, Kunming University of Science and Technology, Kunming, Yunnan 650500, China
3. Department of Civil Engineering, Yunnan University, Kunming, Yunnan 650500, China

Abstract: In order to study the influence of joint density on the strength characteristics and failure modes of rock mass, the rock-like specimens with different joint densities were prepared by using 3D sand printing, with the quartz sand and furan resin being employed as the printing materials. The uniaxial compression test was performed on the 3D sand printed specimens, and the digital image correlation (DIC) method was used as a non-contact technique to monitor the full-field deformation. The crack initiation, propagation and coalescence behaviors were quantitatively analyzed from the micromechanics point of view. The results show that the shape of stress-strain curve and the compressive-to-tensile strength ratio of 3D sand printed intact specimen are similar with those of the natural rock, which can be grouped as a rock-like material. The variation processes of stress-strain curves with different joint densities are similar, and can be divided into initial compaction, linear elastic deformation, crack development and residual strength stages. The mechanical properties of specimens decrease with the increase of joint density ε_f, and the relationship can be expressed as exponential decay functions. By calculating the strain field and displacement vector distribution on the specimen surface, the deformation field distribution and crack propagation of the specimen are found to be closely related to the joint density. The failure mode shifts from axial tension failure (ε_f = 0.280%) toward mixed failure (ε_f = 1.193%) and then to tensile coalescence band failure ($\varepsilon_f \geqslant$ 1.712%) as the flaw density increases. When the joint density is greater than or equal to 2.739%, the block rotation appears in the tensile coalescence band, and the bookshelf faulting with block rotation is reproduced.

Keywords: rock mechanics; joint density; 3D printing; failure mode; digital image correlation (DIC) method; displacement field

1 Introduction

Geological defects such as faults, joints, and fissures inevitably exist in natural rocks[1]. A large number of engineering examples show that the strength degradation and instability of rocks are often closely related to the initiation, propagation and coalescence of these defects. Therefore, in-depth study of the mechanical properties of jointed rock masses has important theoretical and practical significance for understanding the internal rock bridges in jointed rock slope and the fracture process of jointed rock mass during the excavation of underground caverns to ensure the safety of these rock mass projects[2].

In recent years, many scholars have carried out a series of studies on jointed rock masses. Wong et al.[3], Chen et al.[4], and Yang et al.[5] used gypsum materials to prepare rock-like specimens containing joints, and summarized the effects of joint dip, connectivity, interlayer spacing, and overlap on the failure mode of rock masses. Wang et al.[6] and Yang et al.[7] conducted uniaxial and triaxial compression tests on cement mortar specimens containing joints, and explored the mechanical properties of specimens under different joint inclinations, numbers and roughness. Zhang et al.[8] used an independently developed rock-like material to prepare model specimens with cross-cracks. Li et al.[9] used iron powder and quartz sand as aggregates, barite powder as a regulator, and rosin and alcohol as a binder to prepare similar material models, and analysed the instability characteristics of jointed rock masses during excavation. However, the above experimental studies rarely involve the effect of joint density that is an indicator widely used to evaluate the structural characteristics of engineering rock masses[10]. Moreover, the preparation of rock-like specimens is mainly manual pouring, and thus it is difficult to ensure the accuracy and repeatability[11].

3D printing technology has the outstanding advantage of accurate replication of complex structural models, which provides a new method for solving the above-mentioned challenges in the preparation of rock specimens. In recent years, scholars have mainly adopted the following three

Received: 17 November 2020 Revised: 8 February 2021
This work was supported by the National Natural Science Foundation of China(11902128, 41762021) and the Applied Basic Research Foundation of Yunnan Province (2019FI012).
First author: QI Fei-fei, male, born in 1994, Postgraduate, majoring in rock mechanics and engineering. E-mail: kmust_qifeifei@163.com
Corresponding author: ZHANG Ke, male, born in 1986, PhD, Associate Professor, PhD supervisor, mainly engaged in the teaching and research of rock mechanics and engineering. E-mail: zhangke_csu@163.com

types of printing technologies:

(1) Extrusion type: Jiang et al.[12] used polylactic acid material (PLA) as the printing material, and explored the application of fused deposition modelling (FDM) technology to the specimen production for rock mechanics investigation, and found out that PLA material exhibits plastic deformation characteristics, which are very different from the mechanical properties of natural rocks. Wang et al.[13], Zhang et al.[14], Jin et al.[15] and others used FDM technology to print joint models with complex shapes, and then poured a rock-like matrix with cement mortar, which provided a new way for the preparation of rock-like specimens containing joints.

(2) Photopolymerization type: Ju et al.[16] adopted stereolithography (SLA) and CT scanning technology to reproduce coal and rock mass models with complex internal structural features by using photosensitive resin as the printing material. The specimens printed by SLA technology have fine structure and high strength, but the intact photosensitive resin specimens have poor brittleness[17].

(3) Powder type: Jiang et al.[18] printed rock-like specimens containing joints and holes based on gypsum materials, and found out that the crack propagation process is in good agreement with real rocks, but this type of specimen is suitable to simulate low-strength rocks. Tian et al.[19] initially explored the application of 3D sand printing technology in rock mechanics testing, and believed that compared with other 3D printed specimens, sand specimens have mechanical properties highly similar to sandstone.

Based on this, this paper uses 3D sand printing technology to prepare rock-like specimens containing joints. The effect of joint density is considered and a uniaxial compression test is carried out. The digital image correlation (DIC) method is used to quantitatively analyse the global strain field and displacement field from the perspective of micromechanics, which contributes to gain a better understanding of the deformation and failure mechanism of jointed rock masses. The corresponding results have certain reference value for the application of 3D sand printing technology in rock mechanics testing.

2 3D printing of jointed rock-like specimens

2.1 Printing equipment and printing materials

The ExOne S-MAXTM 3D sand printer was used to print rock-like specimens (see Fig.1). The maximum formable size of the equipment is 1 800 mm×1 000 mm×700 mm, the printing layer thickness ranges from 0.26 to 0.38 mm, and the printing accuracy is 0.1 mm. In this study, artificial quartz sand and furan resin glue were used as printing materials, and the self-hardening process of furan resin and quartz sand was undertaken for printing at the room temperature. The particle size of artificial quartz sand is uniformly distributed between 0.074 mm and 0.147 mm, and the main mineral component is SiO_2, as shown in Fig.2. Furan resin is a thermosetting resin adhesive that has the characteristics of fast curing speed and high brittleness[20].

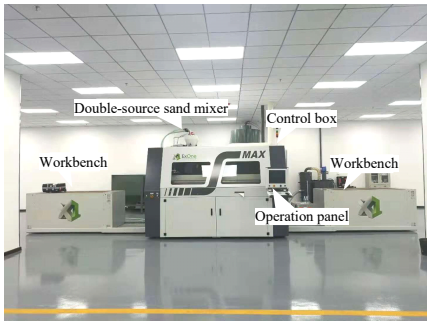

Fig. 1 S-MAX 3D sand printer

Fig. 2 Artificial quartz sand

2.2 Specimen design

In rock mass engineering, the joint density ε_f is an important indicator of the degree of joint development. This article defines it as the percentage of the joint area in the unit measurement area. The measurement area is the cross section perpendicular to the strike of the joint plane:

$$\varepsilon_f = \frac{\sum_{i=1}^{n} s_i}{S} \times 100\% \quad (1)$$

where n is the total number of joints in the measurement area; s_i is the area of the i-th joint in the measurement area; and S is the total area of the measurement area.

The size of the specimen is designed as 100 mm×100 mm×20 mm (height×width×thickness). The prefabricated joints are arranged in echelon form and having

thickness penetrating the specimen, as shown in Fig.3. Since the influence of geometric parameters such as joint dip, connectivity rate, and interlayer spacing on the fracture behavior of rock mass have been systematically studied[3−9], this article focuses on the influence of joint density. In order to simplify the test conditions, let the joint length L_j = 20 mm, the joint width B = 1.4 mm, and the joint spacing S equals the length of rock bridge L_r. Field investigations found that joints with low dip angles are exposed in many rock engineering projects and are prone to induce geological disasters[21], so the joint dip angle is set to be 30º in this experiment. The length of the rock bridge is taken as 65, 35, 30, 25, and 20 mm, the corresponding joint density ε_f is 0.280%, 1.193%, 1.712%, 2.739%, and 3.113%. In addition, specimens without joints (ε_f = 0%) are designed for comparison.

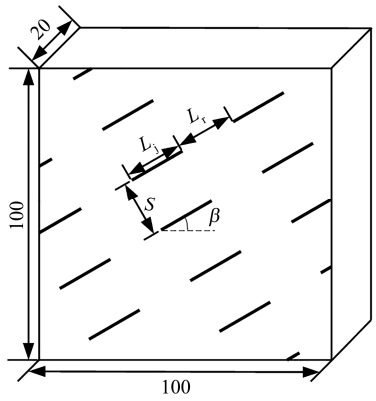

Fig. 3 Geometrical parameters of joint distribution(unit: mm)

In order to analyse the mechanical properties of the intact 3D printed specimens, two groups of standard cylindrical specimen were also prepared: (a) size ϕ 50 mm× 100 mm (diameter×height), used for uniaxial compression test; (b) size ϕ50 mm×50 mm (diameter×height), used for Brazil splitting test. Three identical specimens were prepared for each group.

2.3 3D printing process

The specimen 3D printing process is as follows: (i) Use AutoCAD to build a 3D digital model of the sample, export the *.STL standard format file, and import it into the S-MAX 3D sand printer. (ii) Place the quartz sand and furan resin cement in the powder feeding cylinder and the cement supply cylinder separately. The printing layer thickness is set to 0.3 mm in order to ensure the moulding quality of the specimen. (iii) The 3D sand printer performs layered printing by laying a layer of sand and spraying a layer of adhesive from the bottom up. The printed specimen is shown in Fig.4. It should be noted that the 3D printed specimens exhibit anisotropy, and the printing direction will affect the mechanical properties of the specimens[19]. Therefore, this study uniformly stipulates that the Z-axis direction (that is, the thickness direction of the specimen) is set as the printing layer stacking direction, as shown in Fig.5.

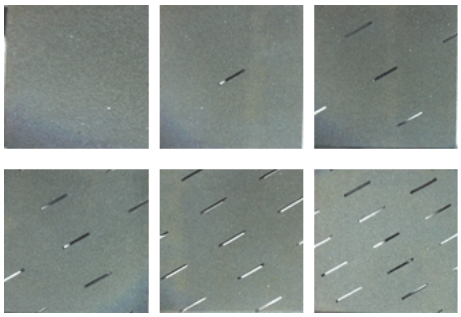

(a) Rock-like specimens with different joint densities

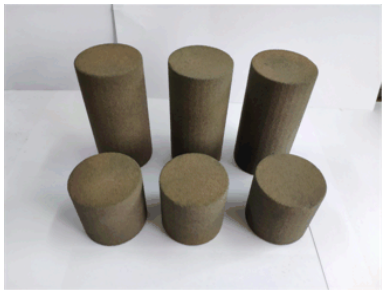

(b) Standard size rock-like specimen

Fig. 4 3D sand printed specimens

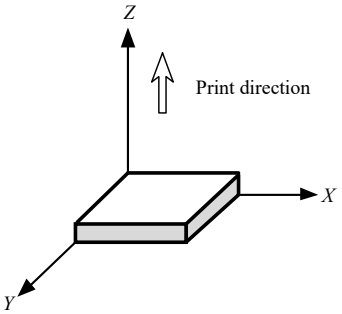

Fig. 5 Work direction of 3D printing

3 Test design and mechanical properties of rock-like specimens

3.1 Test apparatus

The schematic diagram of the testing system is shown in Fig.6. The uniaxial compression test was carried out using the WDW-100 testing device developed by Jinan Shijin Group Co., Ltd. The loading method is displacement control, and the loading rate is 0.3 mm/min. During the experiment, an industrial camera was used to collect digital speckle images, with a resolution of 2 592 pixels × 1 944 pixels, and a collection rate of 1 frame/s. An LED light

was placed next to the camera to ensure that the captured digital image has sufficient brightness and contrast.

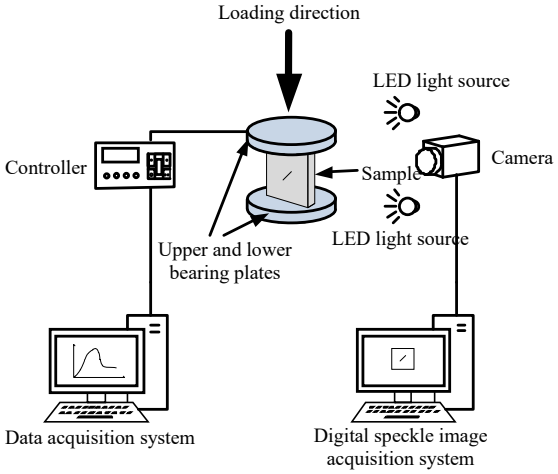

Fig. 6 Testing system

3.2 Artificial speckle field processing and test process

The sample processing and testing procedures are as follows: (i) Spray a layer of white paint uniformly on the front of the sample, spray black paint after drying to form a random artificial speckle field as a carrier of deformation information. (ii) Before the test, place the sample between the upper and lower bearing plates, install and adjust the digital image acquisition equipment. (iii) Acquire the digital speckle image on the front of the sample in real time during the test. (iv) Stop collecting data after the test is over, and import the speckle images into the DIC processing software Ncorr[22] and calculate the displacement fields and strain fields during the loading process of the specimen.

3.3 Mechanical properties

The test results of intact rock-like samples are shown in Table 1. The elastic modulus is defined as the slope of the straight-line section in the elastic deformation stage. In the table, samples 1 to 3 are used for uniaxial compression test, and samples 4 to 6 are used for Brazil splitting test. It can be seen from the table that the coefficients of variation of uniaxial compressive strength, elastic modulus and tensile strength are 0.018, 0.003, and 0.017, respectively. This shows that the rock-like specimens prepared by 3D sand printing technology have stable mechanical properties and sound repeatability. The compression-tensile strength ratio of the intact specimen is 13.8, indicating that it has distinct characteristic of brittle materials.

Table 1 Statistical results of mechanical properties of rock-like specimens

Test category	Sample No.	Strength /MPa	Elastic modulus /GPa	Strength		Elastic modulus	
				Average Value /MPa	Coefficient of variation	Average value /MPa	Coefficient of variation
Uniaxial compression	1	8.43	1.15	8.26	0.018	1.15	0.003
	2	8.23	1.14				
	3	8.13	1.16				
Brazil Splitting	4	0.59	—	0.60	0.017	—	—
	5	0.60	—				
	6	0.61	—				

Typical stress−strain curves of 3D sand-printed rock specimens are illustrated in Fig.7. The stress−strain curve of the specimen under uniaxial compression can be roughly divided as follows (Fig.7(a)): the initial compaction stage (oa_1 section) with concaved curve; the elastic deformation stage (a_1b_1 section) with curve being an approximately oblique straight line; the plastic deformation stage (b_1c_1 section) with curve, of which slope dwindles gradually; and the post-peak failure stage (c_1d_1 section) with the stress dropping rapidly after reaching the peak point. At the final stage, the specimen has lost the bearing capacity and shows significant brittle failure characteristics. Figure 7(b) shows that the stress−strain curve from Brazilian splitting test has experienced compaction (oa_2 section), elastic deformation (a_2b_2 section) and post-peak failure (b_2c_2 section) successively, and there is no obvious plastic deformation. Therefore, it can be summarised that the

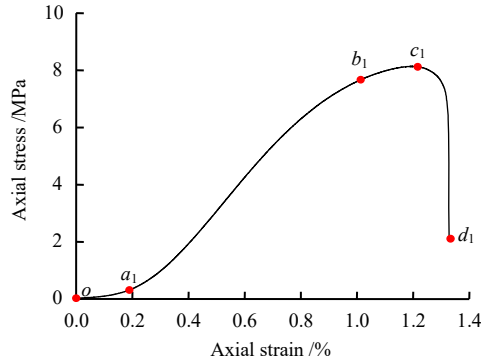

(a) Uniaxial compression test

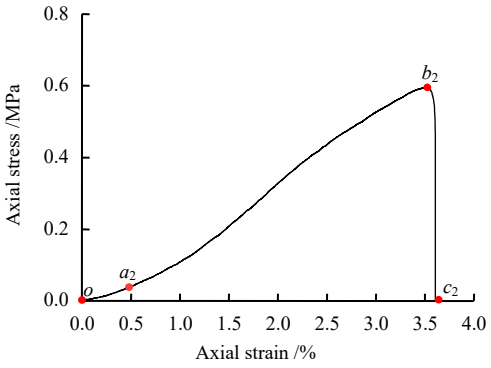

(b) Brazilian splitting test

Fig. 7 Stress−strain curves of typical rock-like specimens

mechanical properties of the 3D printed specimen are similar to those of real rocks, and can be regarded as a rock-like material, which can be applied to the experimental research on rock mechanics.

4 Effect of joint density

4.1 Strength and deformation parameters

Figure 8 shows the compressive strength σ_p and elastic modulus E of specimens with different joint densities under uniaxial compression. Fitting analysis of these test data are performed with the equations derived as follows:

$$\sigma_p = 7.46\mathrm{e}^{-\varepsilon_f/1.91} + 0.63 \quad (R^2 = 0.98) \tag{2}$$

$$E = 0.94\mathrm{e}^{-\varepsilon_f/0.97} + 0.43 \quad (R^2 = 0.98) \tag{3}$$

It can be seen that increasing the joint density will cause the deterioration of the specimen mechanical properties; the relationship between the strength deformation parameters and the joint density is exponentially attenuated, and the correlation coefficient R_2 is both 0.98. Shu et al.[23] and Shi et al.[24] conducted experiments and numerical simulations on jointed rock masses, and found that the compressive strength, elastic modulus and the number of joints also show a nonlinear attenuation correlation,

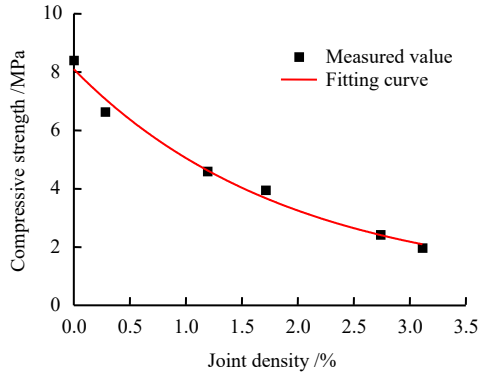

(a) Compressive strength

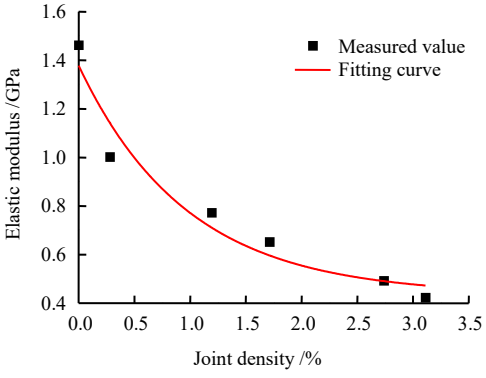

(b) Elastic modulus

Fig. 8 Relationship between joint density and mechanical properties

and the attenuation amplitude varies with the number of joints; the attenuation gradually slows down with the increase of the joint number. Change of the number of joints results in the change of the joint density, so the conclusions of this paper can be considered similar to the conclusions obtained by Shu et al.[23] and Shi et al.[24]

4.2 Deformation and fracture evolution

The digital image correlation method is a non-contact and non-destructive monitoring method based on image processing and numerical calculation. Its basic principle is to analyse the digital speckle images before and after the deformation of the specimen surface through the image matching and tracking methods where the movement of the geometric points are tracked, and the deformation field on the surface of the specimen is calculated[25]. In this study, the digital image correlation software Ncorr was used to calculate the strain field during the loading process of the specimen. The basic algorithms include the sub-zone deformation, nonlinear optimization, reliability guidance and strain calculation, and the strain error is less than 0.05%[22].

4.2.1 Strain field at the initial stage of loading

Nephograms of the horizontal and vertical strain fields of specimens with different joint densities are presented when the axial strain is 0.2%. The joint density significantly affects the deformation field distribution of the specimen at the initial stage of loading. When the joint density ε_f = 0.280%, 1.193% and 1.712%, the strain field distribution on the surface of the specimen is relatively uniform, and the corresponding values are also very low. However, under the same axial strain level, some strain localized bands have begun to appear around the joints of the specimen when the joint density ε_f = 2.739% and 3.113%.

The maximum relative strain is defined as the difference between the maximum value and the minimum value of the global strain, and it is used to characterize the degree of strain differentiation of the specimen; the larger the value, the more significant the strain concentration. Figure 10 shows the maximum relative strain of specimens with different joint densities when the axial strain is 0.2%. It can be seen from the figure that as the joint density increases, the maximum relative strain shows an increasing trend, which means that the degree of strain differentiation around the joint is intensified, which also explains the attenuation of macro-mechanical parameters.

4.2.2 Relationship between stress−strain curve and crack propagation

With the change of joint density, the failure modes

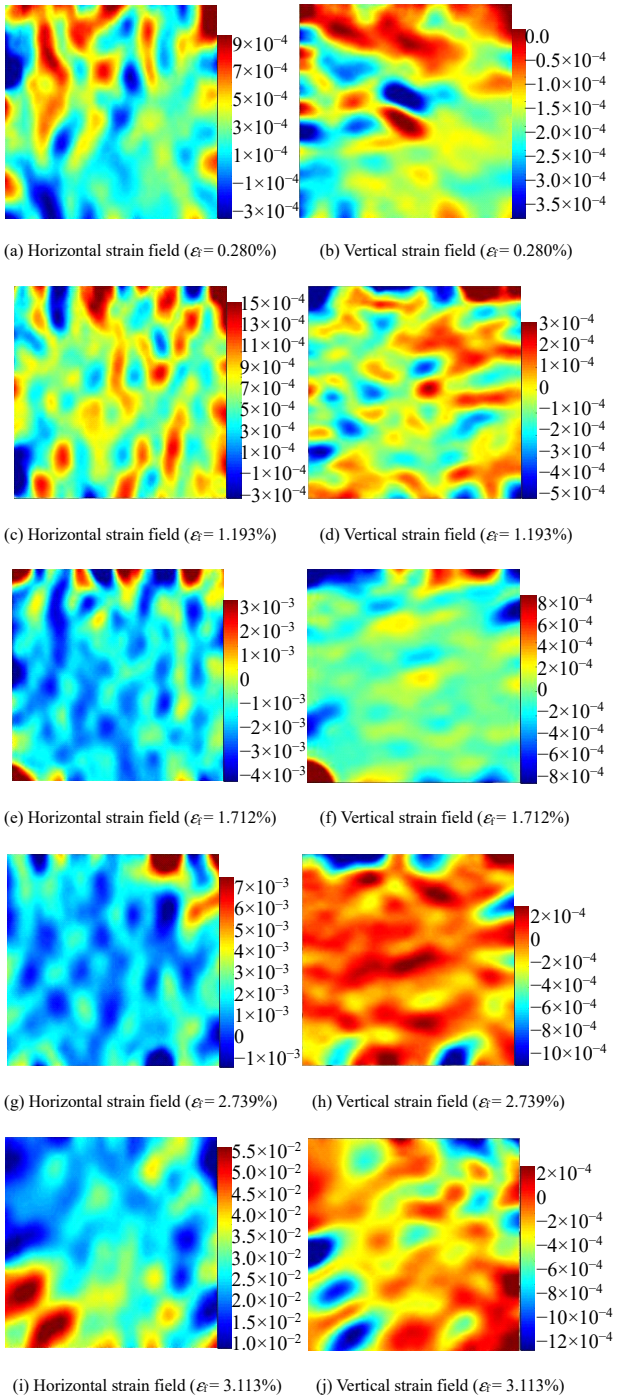

(a) Horizontal strain field (ε_1= 0.280%) (b) Vertical strain field (ε_1= 0.280%)

(c) Horizontal strain field (ε_1= 1.193%) (d) Vertical strain field (ε_1= 1.193%)

(e) Horizontal strain field (ε_1= 1.712%) (f) Vertical strain field (ε_1= 1.712%)

(g) Horizontal strain field (ε_1= 2.739%) (h) Vertical strain field (ε_1= 2.739%)

(i) Horizontal strain field (ε_1= 3.113%) (j) Vertical strain field (ε_1= 3.113%)

Fig. 9 Strain fields at an axial strain of 0.2%

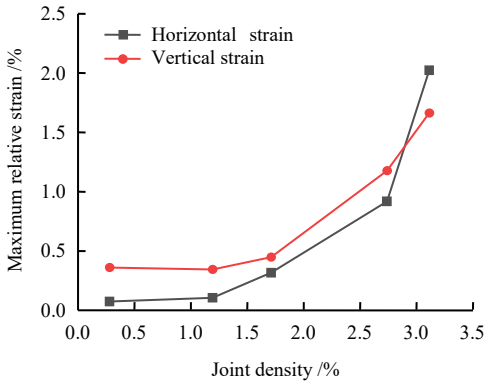

Fig. 10 Relationship between joint density and maximum relative strain

of the specimens can be classified into three categories: axial tensile failure, tensile−coalescence band failure, and mixed failure, denoted as modes I, II, and I-II, respectively. The stress−strain curves of typical specimens corresponding to each failure mode are shown in Figs. 11(a), 12(a) and 13(a). The five stress levels during the loading process of these specimens are selected for identification, which

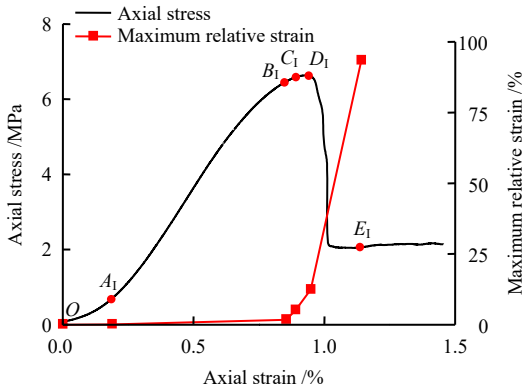

(a) Stress−strain curve and maximum relative strain

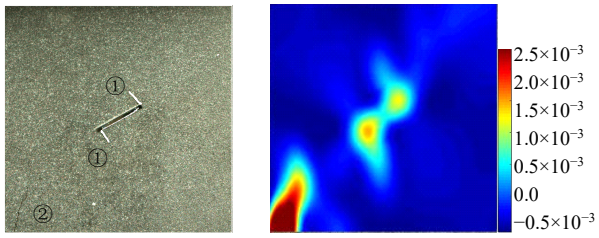

(b) Crack propagation (mark point B_1) (c) Nephogram of horizontal strain field (mark point B_1)

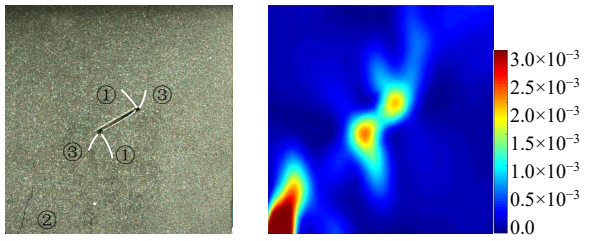

(d) Crack propagation (mark point C_1) (e) Nephogram of horizontal strain field (mark point C_1)

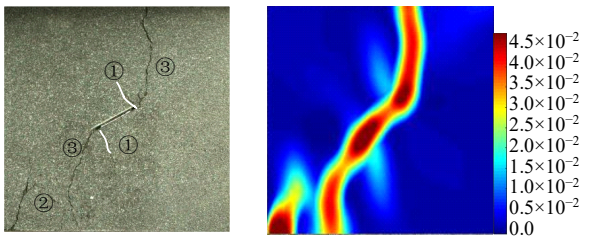

(f) Crack propagation (mark point D_1) (g) Nephogram of horizontal strain field (mark point D_1)

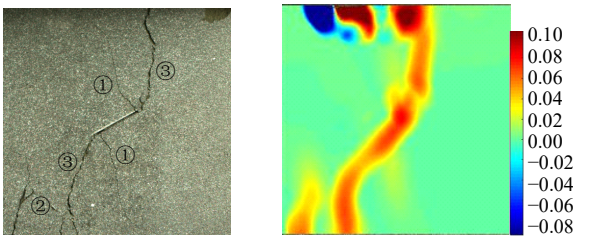

(h) Crack propagation (mark point E_1) (i) Nephogram of horizontal strain field (mark point E_1)

Fig. 11 Stress−strain curve, maximum relative strain, crack propagation and strain field during loading process (model I)

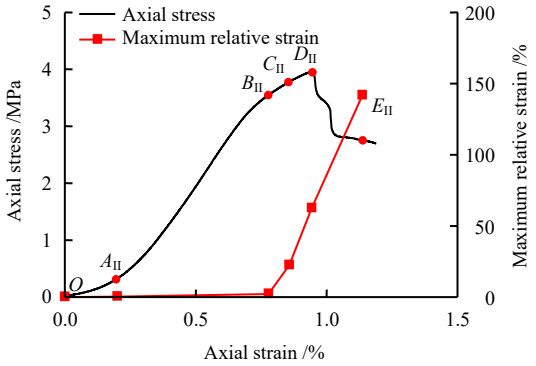

(a) Stress−strain curves and maximum relative strain

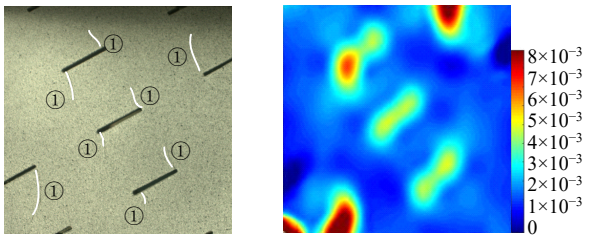

(b) Crack propagation (mark point B_{II}) (c) Nephogram of horizontal strain field (mark point B_{II})

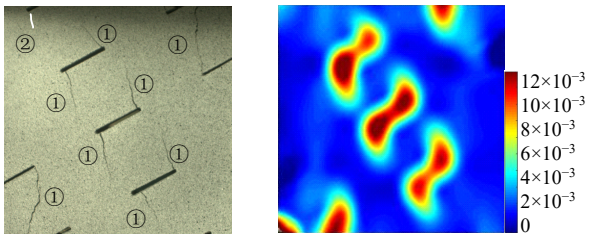

(d) Crack propagation (mark point C_{II}) (e) Nephogram of horizontal strain field (mark point C_{II})

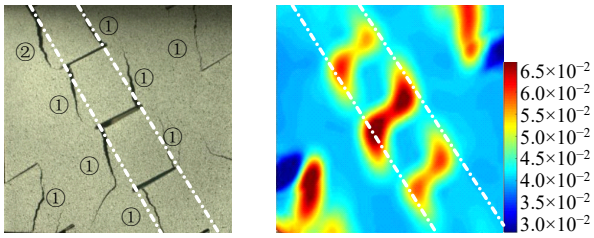

(f) Crack propagation (mark point D_{II}) (g) Nephogram of horizontal strain field (mark point D_{II})

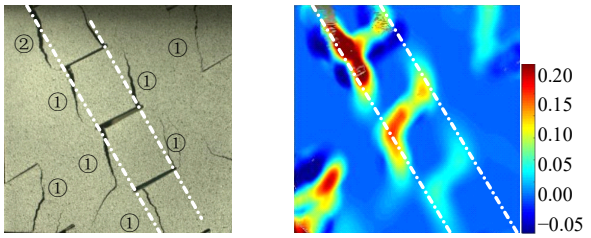

(h) Crack propagation (mark point E_{II}) (i) Nephogram of horizontal strain field (mark point E_{II})

Fig. 12 Stress−strain curve, maximum relative strain, crack propagation and strain field during loading process(model II)

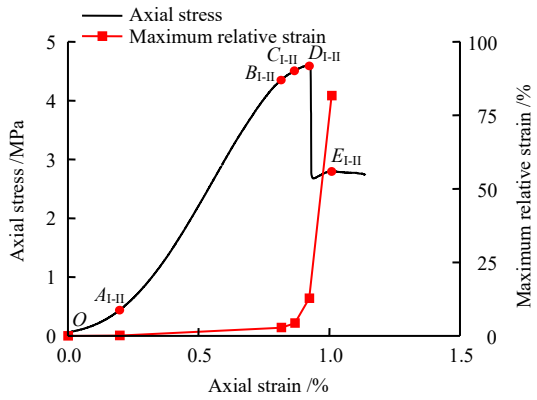

(a) Stress−strain curves and maximum relative strain

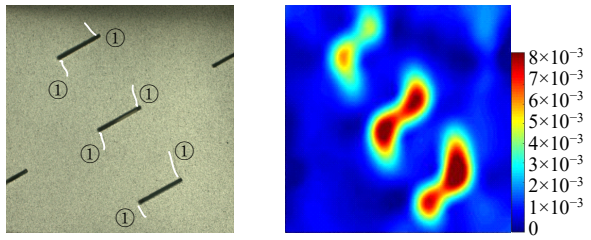

(b) Crack propagation (mark point B_{I-II}) (c) Nephogram of horizontal strain field (mark point B_{I-II})

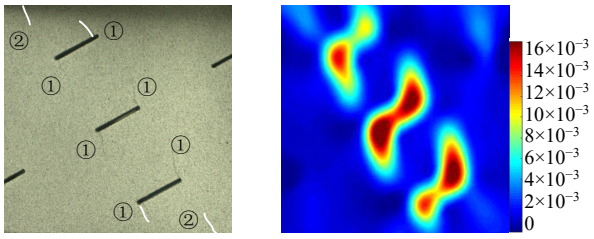

(d) Crack propagation (mark point C_{I-II}) (e) Nephogram of horizontal strain field (mark point C_{I-II})

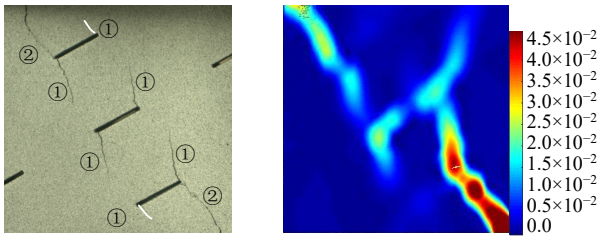

(f) Crack propagation (mark point D_{I-II}) (g) Nephogram of horizontal strain field (mark point D_{I-II})

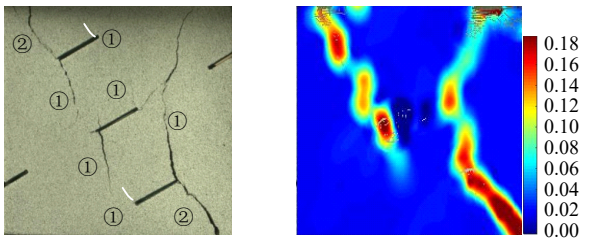

(h) Crack propagation (mark point E_{I-II}) (i) Nephogram of horizontal strain field (mark point E_{I-II})

Fig. 13 Stress−strain curve, maximum relative strain, crack propagation and strain field during loading process (model I-II)

are marked as *A*, *B*, *C*, *D*, and E, and the corresponding subscripts I, II, or I-II represent the failure mode types. Point *A* corresponds to the initial stage of loading. At this time, the axial strain is 0.2%, and no cracks appear on the surface of the specimen. The strain field calculation results are shown in Fig.9. Points *B*, *C*, *D*, and *E* correspond to the crack initiation, crack propagation, peak stress, and residual stress, respectively. Figures 11(b)−11(g), 12(b)−12(g) and 13(b)−13(g) respectively show

the crack growth and the horizontal strain field corresponding to the typical mark points *B*, *C*, *D*, and *E*, and new cracks are numbered with circled numbers in the order of appearance.

(1) Mode I: axial tensile failure

When the joint density ε_f = 0.280%, the specimen contains only one prefabricated joint, and the corresponding stress−strain curve, crack propagation process and nephogram of horizontal strain fields are shown in Fig.11. When the load reaches 97.39% of the peak stress corresponding to the mark point B_I in Fig.11(a), the new crack ① originates at the tip of the prefabricated joint at the earliest, and the propagation direction is approximately perpendicular to the joint, as shown in Fig.11(b). The strain field calculation results indicate that there are strain localization bands around the joint and at the two tips, as shown in Fig.11(c). At the same time, a crack ② and a corresponding strain localization zone appear in the lower left corner of the specimen. It should be pointed out that the cracks ① and ② stop after extending for a certain length, so they do not play a leading role in the final damage. When continuing to load to 99.53% of the peak stress, which is marked as point C_I in Fig.11(a), cracks ③ and corresponding strain localization zones begin to appear at the joint tip along the nearly axial direction, as shown in Figs. 11(d) and 11(e). When the axial load reaches the peak value, that is, the mark point D_I in Fig.11(a), the crack ③ and the corresponding strain localization zones join and coalesce the specimen, as shown in Figs. 11(f) and 11(g). The test results are consistent with the uniaxial compression test results of single-joint marble from Yuan et al.[25]. Finally, the stress−strain curve drops to the residual strength and tends to be stable, as illustrated by the mark point E_I in Fig.11(a). At this time, the crack penetration path does not change, but the strain field value increases, as shown in Figs. 11(h) and 11(i).

(2) Mode II: tensile-coalescence band failure

The crack propagation processes are similar when the joint density ε_f = 1.712%, 2.739%, 3.113%, so the specimen with ε_f = 1.712% is selected to provide a typical analysis, as shown in Fig.12. When it is loaded to 89.99% of the peak stress, which is marked as point B_{II} in Fig.12(a), cracks ① and the corresponding strain localization zones first appear at the tip of the precast joint, as shown in Figs.12(b) and 12(c). Similar to the cracks ① that appear in mode I. When continuing to load to 95.82% of the peak stress, that is, at the mark point C_{II} in Fig.12(a), a crack ② occurs at the upper left corner of the specimen. When the axial load reaches the peak value corresponding to the mark point D_{II} in Fig.12(a), the crack ② overlaps with the left tip of the nearest joint, and the cracks ① and ② interact with the precast joints to form one or more tensile-coalescence bands perpendicular to the joint direction, which appear as strain localized bands covering the tensile-coalescence bands on the nephogram of the strain field, as shown on Figs. 12(f) and 12(g). Finally, the specimen enters the post-peak residual stress stage, which is the mark point E_{II} in Fig.12(a). The crack penetration path has not changed, but the strain concentration is more significant, as shown in Figs. 12(h) and 12(i).

(3) Mode I-II: mixed failure

When the joint density ε_f = 1.193%, the specimen shows mixed failure, and the corresponding stress−strain curve, crack propagation process and nephogram of horizontal strain fields are shown in Fig.13. Figures 13(b)−13(g) demonstrate the evolution processes of cracks ① and ②, corresponding to the mark points $B_{I–II}$−$D_{I–II}$ in Fig.13(a), are close to that of Mode II. As the axial load continues to increase, as shown in Fig.13(h), the crack at the right tip of the joint at the bottom of the specimen does not overlap with the tip of the adjacent joint, but expands in the nearly axial direction. Eventually, it penetrates the upper end of the specimen, which corresponds to the marked points E_{I-II} in Fig.13(a); the horizontal strain field nephogram also shows a strain localized zone penetrating the specimen, as indicated in Fig.13(i). Cracks ① and ② constitute the macroscopic fracture surface and dominate the final failure mode of the specimen.

4.2.3 Evolution of maximum relative strain

For different failure modes, the calculation results of the maximum relative strain corresponding to the mark point of each typical specimen are shown in Figs. 11(a), 12(a) and 13(a). It can be found from the figure that before mark point *B*, the maximum relative strains of the specimens with different joint densities show a gentle growth trend. This can be explained that the specimens are in an elastic deformation state and the overall deformation is relatively uniform. After the crack initiation and propagation, the resistance structure of the specimen undergoes abrupt changes, and the rock matrix surrounding the cracks also undergo strain adjustment, resulting in a sudden increase in the maximum relative strain.

4.3 Mechanism of crack propagation

4.3.1 Principle of displacement vector solution

By calculating the displacement field of the specimen

surface using Ncorr[22], the matrices of horizontal displacement field and vertical displacement field are derived, then Matlab is used to solve for the displacement vector diagram during the loading process. Suppose the coordinates of any geometric point on the digital image before deformation are (x, y), and the coordinates after deformation are (x', y'), and the vector solution formula is

$$\left.\begin{aligned} l &= \sqrt{(x'-x)^2+(y'-y)^2} \\ \alpha &= \arctan\frac{\Delta y}{\Delta x} = \arctan\frac{(y'-y)}{(x'-x)} \end{aligned}\right\} \quad (4)$$

where l is the total displacement of the geometric point; α is the angle between the direction of the displacement vector of the geometric point and the positive x direction, and the rightward direction on the x-axis is designated to be positive.

4.3.2 Calculation results and analysis

The calculation results of typical local displacement vectors amid the crack propagation are shown in Figs. 14−16. This displacement information represents the accumulated displacement vectors of the speckles (i.e. meso-particles). Especially when cracks are initiating and expanding, the direction and magnitude of the displacement vector of surrounding meso-particles will change significantly. Using these changes, the damage mechanism

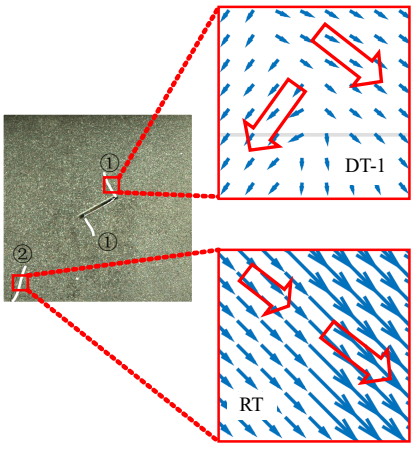

(a) Mark point B_{I}

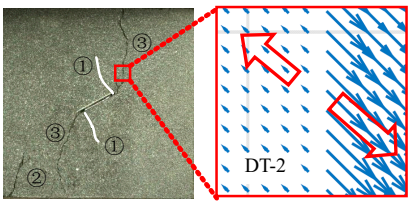

(b) Mark point D_{I}

Fig. 14 Displacement vector distribution during crack propagation process (model I)

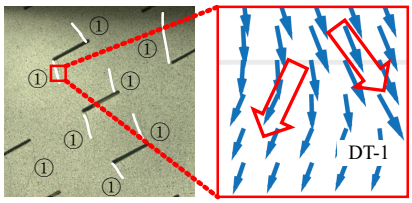

(a) Mark point B_{II}

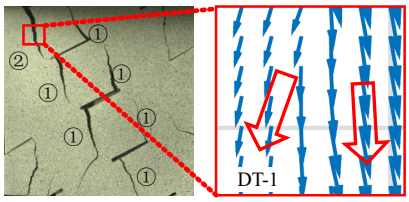

(b) Mark point D_{II}

Fig. 15 Displacement vector distribution during crack propagation process(model II)

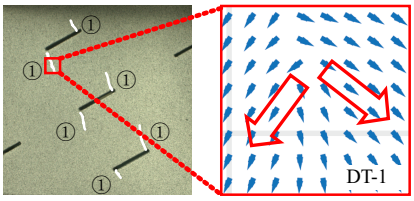

(a) Mark point $B_{\mathrm{I\text{-}II}}$

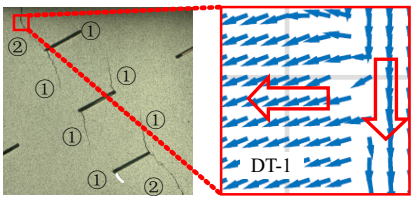

(b) Mark point $D_{\mathrm{I\text{-}II}}$

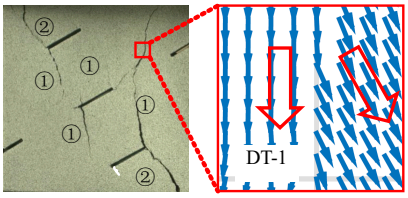

(c) Mark point $E_{\mathrm{I\text{-}II}}$

Fig. 16 Displacement vector distribution during crack propagation process (model I-II)

can be revealed from the perspective of mesomechanics. In this study, three basic cracks were identified:

(1) Direct tensile crack (denoted as DT-1): The meso-particles on both sides of the newly generated crack move away from each other at a certain angle (Fig.14(a), Fig.15).

(2) Direct tensile cracks (denoted as DT-2): The meso-particles on both sides of the newly generated cracks move away from each other.

(3) Relative tensile cracks (denoted as RT): The meso-particles on both sides of the newly generated crack move in the same direction, but the displacement of one side

is significantly larger than that of the other side, causing the meso-particles on both sides to produce relative displacement and separation.

The results of the crack identification in different failure modes are summarized in Table 2.

Table 2 Summary of crack classification with different failure modes

Mode	Crack①	Crack②	Crack③
I	DT-1	RT	DT-2
II	DT-1	DT-1	—
I-II	DT-1	DT-1	—

It should be noted that for Mode II, different joint densities will lead to different motion characteristics of the block in the tension-coalescence zone, and the corresponding typical block displacement vector distribution is shown in Fig.17. When $\varepsilon_f = 1.712\%$, the movement direction of the block is basically the same as the overall deformation direction of the specimen. When $\varepsilon_f \geqslant 2.739\%$, the block rotates clockwise, which basically match with the numerical simulation results of particle flow of densely jointed rock specimens[26]. This result is also similar to the domino-type structure, that is, the phenomenon of bookshelf fault with block rotation[27], as shown in Fig.18. From the calculation results leveraging digital image processing techniques in this paper, this geological structure is mainly formed under tension. The next step will be

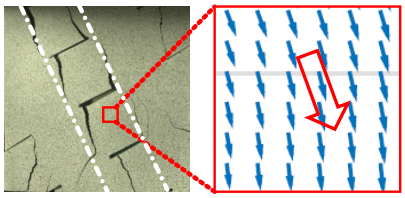

(a) $\varepsilon_f = 1.712\%$

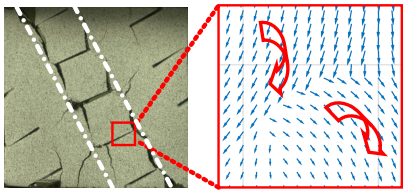

(b) $\varepsilon_f = 2.739\%$

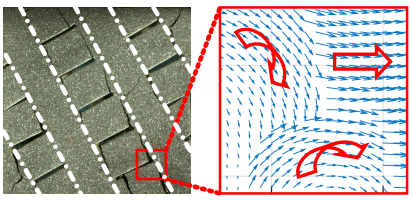

(c) $\varepsilon_f = 3.113\%$

Fig. 17 Displacement vectors of blocks for model II

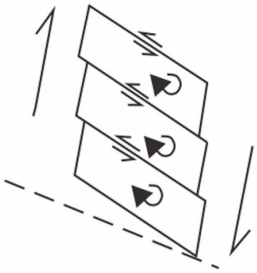

Fig. 18 Bookshelf fault with block rotation[27]

to conduct a comprehensive and systematic study on this topic in order to obtain universally significant research conclusions.

5 Conclusion

In this paper, 3D sand printing with digital image correlation technologies were combined to reproduce the macro-mechanical properties of jointed rock masses during the loading process and to study the influence of joint density from the perspective of physical experiments, and the fracture mechanism of rock masses containing different joint densities was also revealed from the perspective of mesomechanics. The following conclusions were obtained:

(1) Unlike the previous 3D printing technologies based on a single material, the specimen produced by the 3D sand printing technology is a composite material—the quartz sand of one of the printing materials is similar to the mineral particles in the rock, and the other printing material Furan resin, resembles the cementing component in rock. The test results of the basic mechanical parameters of the intact 3D printed specimen show that the coefficient of variation is less than 0.018, and the compression-tension strength ratio is 13.8. Therefore, in consideration of material composition and mechanical properties, 3D sand printed specimens are more suitable for simulating rocks while can ensure the repeatability of test results.

(2) The 3D sand printing technology is introduced in this paper to prepare rock-like specimens containing parallel joint groups. The significant manufacturing advantages help solve the problems of low accuracy and lack of repeatability faced by traditional specimen preparation. It provides a reliable physical model for the study of the fracture mechanism of jointed rock masses. The study found that the existence of joints deteriorates the mechanical properties of the specimens, and as the density of joints increases, the compressive strength and elastic modulus of the specimens decrease exponentially.

In the next step, the effects of joint inclination and complex joint network will be explored.

(3) The digital image correlation method is used to realize real-time, non-contact full-field monitoring of the specimen loading process, and in combination with the maximum relative strain, the evolution of the strain field and strain localization zone during the specimen loading process are quantitatively studied. The failure mode of the specimen is closely related to the joint density, and can be classified as axial tensile failure, tensile-coalescence failure and mixed failure.

(4) When the crack initiates, propagates and coalesces, the displacement near the crack appears to be discontinuous, and different movement directions are demonstrated by the displacement vector. This paper quantitatively studies the incubation and evolution process of new cracks from the perspective of mesomechanics, and identifies three basic cracks, namely two direct tensile cracks (denoted as DT-1 and DT-2) and relative tensile crack (denoted as RT). The bookshelf faulting with block rotation in the geological structure is reproduced in the laboratory when $\varepsilon_f \geqslant 2.739\%$, a tension-coalescence zone appears in the specimen, and the block in the zone rotates while the corresponding compressive strength reaches the lowest. Displacement vector analysis provides an effective method for in-depth understanding of the mechanical mechanism of the fracture evolution of jointed rock masses.

References

[1] CHEN Wei-zhong, YANG Jian-ping, ZOU Xi-de, et al. Research on macromechanical parameters of fractured rock masses[J]. Chinese Journal of Rock Mechanics and Engineering, 2008, 27(8): 1569−1574.

[2] JIANG Quan, FENG Xia-ting, LI Shao-jun, et al. Cracking-restraint design method for large underground caverns with hard rock under high geostress condition and its practical application[J]. Chinese Journal of Rock Mechanics and Engineering, 2019, 38(6): 1081−1101.

[3] WONG L N Y, EINSTEIN H H. Systematic evaluation of cracking behavior in specimens containing single flaws under uniaxial compression[J]. International Journal of Rock Mechanics and Mining Sciences, 2009, 46(2): 239−249.

[4] CHEN Xin, LIAO Zhi-hong, LI De-jian. Experimental study of effects of joint inclination angle and connectivity rate on strength and deformation properties of rock masses under uniaxial compression[J]. Chinese Journal of Rock Mechanics and Engineering, 2011, 30(4): 781−789.

[5] YANG Xu-xu, JING Hong-wen, TANG Chun-an, et al. Effect of parallel joint interaction on mechanical behavior of jointed rock mass models[J]. International Journal of Rock Mechanics and Mining Sciences, 2017, 92: 40−53.

[6] WANG Pei-xin, CAO Ping, PU Cheng-zhi, et al. Effect of density and inclination of joints on the strength and deformation properties of rock-like specimens under uniaxial compression[J]. Chinese Journal of Engineering, 2017, 39(4): 494−501.

[7] YANG Sheng-qi, LU Jia-wei, TIAN Wen-ling, et al. Experimental study of mechanical behavior of rock specimens with different joint roughness coefficient under conventional triaxial compression[J]. Rock and Soil Mechanics, 2018, 39(Suppl.1): 21−32.

[8] ZHANG Bo, LI Shu-cai, YANG Xue-ying, et al. Uniaxial compression failure mechanism of jointed rock mass with cross-cracks[J]. Rock and Soil Mechanics, 2014, 35(7): 1863−1870.

[9] LI Shu-chen, MA Teng-fei, JIANG Yu-jing, et al. Model tests on deformation and failure laws in excavation of deep rock mass with multiple fracture sets[J]. Chinese Journal of Geotechnical Engineering, 2016, 38(6): 987−995.

[10] YANG Zhong-min, GAO Yong-tao, WU Shun-chuan, et al. Study of the influence of joint parameters on rock mass strength based on equivalent rock mass rechnology[J]. Journal of China University of Mining & Technology, 2018, 47(5): 979−986.

[11] JIN Ai-bing, WANG Shu-liang, WANG Ben-xin, et al. Study on the fracture mechanism of 3D-printed-joint specimens based on DIC technology[J]. Rock and Soil Mechanics, 2020, 41(10): 3214−3224.

[12] JIANG C, ZHAO G. A preliminary study of 3D printing on rock mechanics[J]. Rock Mechanics and Rock Engineering, 2015, 48(3): 1041−1050.

[13] WANG Pei-tao, HUANG Zheng-jun, REN Fen-hua, et al. Investigation of direct shear behavior and fracture patterns of 3D-printed complex jointed models[J]. Rock and Soil Mechanics, 2020, 41(1): 46−56.

[14] ZHANG Ke, QI Fei-fei, CHEN Yu-long. Deformation and fracturing characteristics of fracture network model and influence of filling based on 3D printing and DIC technologies[J]. Rock and Soil Mechanics, 2020, 41(8): 2555−2563.

[15] JIN Ai-bing, WANG Shu-liang, WANG Ben-xin, et al. Fracture mechanism of specimens with 3D printing cross joint based on DIC technology[J]. Rock and Soil Mechanics, 2020, 41(12): 3862−3872.

[16] JU Yang, XIE He-ping, ZHENG Ze-min, et al. Visualization of the complex structure and stress field inside rock by

means of 3D printing technology[J]. Chinese Science Bulletin, 2014, 59(32): 3109−3119.

[17] ZHOU T, ZHU J B. Identification of a suitable 3D printing material for mimicking brittle and hard rocks and its brittleness enhancements[J]. Rock Mechanics and Rock Engineering, 2018, 51(3): 765−777.

[18] JIANG Quan, SONG Lei-bo. Application and prospect of 3D printing technology to physical modeling in rock mechanics[J]. Chinese Journal of Rock Mechanics and Engineering, 2018, 37(1): 23−37.

[19] TIAN Wei, PEI Zhi-ru, HAN Nü. A preliminary research on three-dimensional reconstruction and mechanical characteristics of rock mass based on CT scanning and 3D printing technology[J]. Rock and Soil Mechanics, 2017, 38(8): 2297−2305.

[20] MITRA S, RODRÍGUEZ DE CASTRO A, EL MANSORI M. The effect of ageing process on three-point bending strength and permeability of 3D printed sand molds[J]. The International Journal of Advanced Manufacturing Technology, 2018, 97: 1241−1251.

[21] ZHU Lei, HUANG Run-qiu, CHEN Guo-qing, et al. Mechanical model and evolution of fracture system with a gentle dip angle in rock slope[J]. Rock and Soil Mechanics, 2019, 40(Suppl.1): 53−62.

[22] BLABER J, ADAIR B, ANTONIOU A. Ncorr: open-source 2D digital image correlation Matlab software[J]. Experimental Mechanics, 2015, 55(6): 1105−1122.

[23] SHU J, JIANG L, KONG P, et al. Numerical analysis of the mechanical behaviors of various jointed rocks under uniaxial tension loading[J]. Applied Sciences, 2019, 9(9): 1824.

[24] SHI H, ZHANG H, SONG L, et al. Failure characteristics of sandstone specimens with randomly distributed pre-cracks under uniaxial compression[J]. Environmental Earth Sciences, 2020, 79: 193.

[25] YUAN Yuan, PAN Peng-zhi, ZHAO Shan-kun, et al. The failure process of marble with filled crack under uniaxial compression based on digital image correlation[J]. Chinese Journal of Rock Mechanics and Engineering, 2018, 37(2): 339−351.

[26] YANG S Q, YIN P F, ZHANG Y C, et al. Failure behavior and crack evolution mechanism of a nonpersistent jointed rock mass containing a circular hole[J]. International Journal of Rock Mechanics and Mining Sciences, 2019, 114: 101−121.

[27] LIU Jun, JIA Dong, YIN Hong-wei, et al. Analogue modeling of non-rigid bookshelf fault model in eastern Tibet Plateau[J]. Acta Geologica Sinica, 2020, 94(6): 1780−1792.